RSC Advances

PAPER

View Article Online
View Journal | View Issue

Cite this: *RSC Adv.*, 2024, **14**, 18695

Ruthenium-doped $Ni(OH)_2$ to enhance the activity of methanol oxidation reaction and promote the efficiency of hydrogen production†

Jiajie Lin,[a] Jie Chen,[ab] Changhui Tan,*[ab] Yingzhen Zhang *[cd] and Yancai Li *[ab]

The coupling of the hydrogen evolution reaction (HER) and methanol oxidation reaction (MOR) to produce clean hydrogen energy with value-added chemicals has attracted substantial attention. However, achieving high selectivity for formate production in the MOR and high faradaic efficiency for H_2 evolution remain significant challenges. In light of this, this study constructs an $Ru/Ni(OH)_2$/NF catalyst on nickel foam (NF) and evaluates its electrochemical performance in the MOR and HER under alkaline conditions. The results indicate that the synergistic effect of $Ni(OH)_2$ and Ru can promote the catalytic activity. At an overpotential of only 42 mV, the current density for the HER reaches 10 mA cm^{-2}. Moreover, in a KOH solution containing 1 M methanol, a potential of only 1.36 V *vs.* RHE is required to achieve an MOR current density of 10 mA cm^{-2}. Using $Ru/Ni(OH)_2$/NF as a bifunctional catalyst, employed as both the anode and cathode, an MOR-coupled HER electrolysis cell can achieve a current density of 10 mA cm^{-2} with a voltage of only 1.45 V. Importantly, the faradaic efficiency (FE) for the hydrogen production at the cathode and formate ($HCOO^-$) production at the anode approaches 100%. Therefore, this study holds significant practical implications for the development of methanol electro-oxidation for formate-coupled water electrolysis hydrogen production technology.

Received 22nd March 2024
Accepted 29th May 2024

DOI: 10.1039/d4ra02181a

rsc.li/rsc-advances

1 Introduction

The sustainable development of future energy system requires the support of diverse energy technologies.[1,2] Hydrogen, known for its high energy density, is a promising renewable energy source that has the potential to address both the energy crisis and environmental issues. This has sparked the interest of numerous researchers.[3,4] Water splitting is a prospective way to obtain hydrogen energy, which involves the cathodic hydrogen evolution reaction (HER) and anodic oxygen evolution reaction (OER).[5] However, O_2 is a low-value chemical, which is produced at the anode, and when blended with H_2 produced at the cathode, there is a safety hazard of explosion.[6] Importantly, the OER process requires high energy barriers, which have always limited the industrial application of water electrolysis.

Some studies suggest that employing the methanol oxidation reaction (MOR) with a lower theoretical potential (0.016 V) as a substitute for the high-barrier OER process (theoretical potential of 1.23 V) in traditional water electrolysis could enhance the efficiency and economic value of electrocatalytic hydrogen production.[7] It is noteworthy that methanol, being a simple organic molecule, is readily available, inexpensive, and has low toxicity.[8] Moreover, it is more prone to electrochemical oxidation reactions that can produce formic acid or formate, which are important chemical raw materials.[9] The complexity of formate synthesis, coupled with its huge demand, ensures that the cost per metric ton of formate is four times that of methanol.[10] However, addressing the activity and high selectivity towards formate in the methanol oxidation reaction (MOR) remains a significant challenge.[11] Therefore, the development of efficient bifunctional electrocatalysts is crucial for the advancement of this field.

At present, precious metals (Pt and Pd) and their alloys are still the most effective catalysts for the small molecule oxidation-assisted hydrogen production system.[12,13] However, Ru is less expensive than Pt, which is one of the alternatives to Pt-based catalyst.[14] Thus, new methods may be investigated to increase the use of ruthenium metal and enhance its catalytic oxidizing capacity, which is essential to lower precious metal waste, develop appropriate non-Pt-based catalysts, and enhance their usage. Recently, Feng *et al.*[15] reported the Ru/NC synthesized by hydrothermal and high-temperature calcinations,

[a]*College of Chemistry, Chemical Engineering and Environment, Minnan Normal University, Zhangzhou 363000, P. R. China. E-mail: tanchanghui@mnnu.edu.cn; liyancai@mnnu.edu.cn*

[b]*Fujian Province Key Laboratory of Modern Analytical Science and Separation Technology, Minnan Normal University, Zhangzhou 363000, P. R. China*

[c]*College of Chemical Engineering, Fuzhou University, Fuzhou, 350116, P. R. China. E-mail: 13338287704@163.com*

[d]*School of Chemistry, Chemical Engineering and Biotechnology, Nanyang Technological University, 637457, Singapore*

† Electronic supplementary information (ESI) available. See DOI: https://doi.org/10.1039/d4ra02181a

which can reach 21 mV ultra-low overpotential of HER in 1 M KOH solution; Xu *et al.*[16] reported that the sulfur-doped Ru nanoparticles served as superior catalysts for HER in alkaline media. The catalyst only needs an overpotential of 10 mV to fulfill a current density of 10 mA cm^{-2}. Although the properties of these materials are quite good, the stability still needs to be improved, and these synthesis methods are complex, high-temperature or use hazardous chemicals. Fortunately, self-supporting materials formed *in situ* can reduce the use of binder, not easy to fall off, and increase the stability of the material.[8,17]

Herein, in this study, an Ru-doped $Ni(OH)_2$ self-supported catalyst was synthesized *in situ* on a commercial nickel foam (NF) substrate, denoted as Ru/$Ni(OH)_2$/NF, and its electrochemical performance for HER and MOR was investigated in alkaline conditions. The experimental results demonstrate that the strong synergistic effect between Ru and $Ni(OH)_2$ can enhance the reaction kinetics of HER and MOR, ultimately exhibiting excellent electrocatalytic activity. Assembling Ru/$Ni(OH)_2$/NF as both the cathode and anode in an MOR-coupled HER electrolysis cell required only 1.45 V voltage to achieve a current density of 10 mA cm^{-2}. Importantly, the product of MOR at the anode was high-value formate salts (with a yield of 95%), while the hydrogen evolution rate at the cathode reached 100%, and no O_2 product was detected during the reaction, indicating that this strategy effectively avoids the explosion risk arising from the potential mixing of H_2 and O_2. This work provides certain guidance for efficient and energy-saving hydrogen production coupled with value-added chemical production in alkaline solutions.

2 Experimental section

2.1. Chemicals

The chemicals used in this research were of analytical reagent grade (AR) and were not further purified. Nickel(II) chloride hexahydrate (Puratrem, $NiCl_2 \cdot 6H_2O$, 98%), hydrochloric acid (HCl, 37%), potassium hydroxide (KOH, 85%), *N*,*N*-dimethylformamide (DMF, 99.5%), methanol (CH_3OH, 99.5%) and ethanol (C_2H_5OH, 99.5%) were purchased from Xilong Chemical Co., Ltd. (Shantou, China). NF (110 ppi; mass density of 350 g m^{-2}) was bought from Kunshan New Materials Company (Kunshan, China). Potassium formate ($CHKO_2$, 99%) and ruthenium chloride hydrate ($RuCl_3 \cdot xH_2O$, 98%) were obtained from Macklin Biochemical Co., Ltd. Deionized water from a Milli-Q system was used in all experiments.

2.2. Preparation of the Ru/$Ni(OH)_2$/NF

Firstly, NF was cut to 3 × 2 cm^2, pretreated with 3 M hydrochloric acid for 15 min, and then washed for 15 min with absolute ethanol and deionized water, respectively. Then, $NiCl_2 \cdot 6H_2O$ (40 mg), $RuCl_3 \cdot xH_2O$ (0.1 μmol), DMF (25 mL), ethanol and deionized water (2 mL) were stirred and dissolved. Next, the evenly mixed solution was placed together with ultrasound-treated NF after a hydrothermal process in 90 °C for 12 h. After it was naturally cooled to room temperature, the sample was cleaned with ethanol and water, respectively, to remove the residual reaction liquid, followed by drying at 50 °C overnight.

Additionally, the control samples of Ru/$Ni(OH)_2$/NF-20 and Ru/$Ni(OH)_2$/NF-60 were prepared by a similar method, with the addition of $NiCl_2 \cdot 6H_2O$ 20 mg or 60 mg, respectively.

2.3. Preparation of Ru/NF

$RuCl_3 \cdot xH_2O$ (0.1 μmol), DMF (25 mL), and glacial acetic acid (4 mL) were transferred into a 50 mL Teflon-lined stainless autoclave and heated at 90 °C for 12 h to acquire Ru/NF.

2.4. Preparation of $Ni(OH)_2$/NF

$NiCl_2 \cdot 6H_2O$ (40 mg), DMF (25 mL), ethanol and deionized water (2 mL) were stirred and dissolved, transferred into a 50 mL Teflon-lined stainless autoclave and heated at 90 °C for 12 h to acquire $Ni(OH)_2$/NF.

2.5. Products analysis

The fabricated formate in a two-electrode system were calculated by high-pressure liquid chromatography (HPLC). Potassium formate was used as the standard material for HPLC analysis. 20 μL of the electrolyte was converged and diluted to 1000 μL with deionized water. The eluent was dilute H_2SO_4 (5 mmol L^{-1}), the flow rate was 6 mL min^{-1}, and the column temperature was 35 °C.

The supporting documentation included a full computation of the FE and energy usage as well as details including the electrochemical setup and measurements.

3 Results and discussion

3.1. Structural and composition investigations

As illustrated in Fig. 1A, the Ru/$Ni(OH)_2$/NF catalyst was synthesized in a one-step hydrothermal method under mild conditions. As shown in the SEM image of Ru/$Ni(OH)_2$/NF (Fig. 1B), the external of the NF-covered multitudinous nanosheets presents well-interconnected nanosheet arrays. It can be observed that the $Ni(OH)_2$ nanoplates are vertically grown on NF. These nanosheet arrays link together to one another with diverse voids, more active sites can be exposed, and the structure will be advantageous for the interaction with reactants.[18] Meanwhile, the SEM image of $Ni(OH)_2$ synthesized with different contents of $NiCl_2 \cdot 6H_2O$ are shown in Fig. S1.† Among them, Ru/$Ni(OH)_2$/NF has the best three-dimensional morphology. This distinct hierarchy will make it possible for electrolytes to enter the active site easily and assist in releasing the produced bubbles, thus improving the HER/MOR kinetics by enabling mass transfer.[19] Put differently, a strong structure–activity connection helps to lower the reaction energy barrier and accelerate the kinetics of the reaction.

The crystallinity and phase of Ru/$Ni(OH)_2$/NF were examined using XRD technology. The NF substrate has strong Ni diffraction peaks at 2θ = 44.5°, 51.8°, and 76.4°,[20,21] as shown in Fig. S2.† The low loading of $Ni(OH)_2$ and Ru or the poor crystallinity of the substance or the strong substrate may be

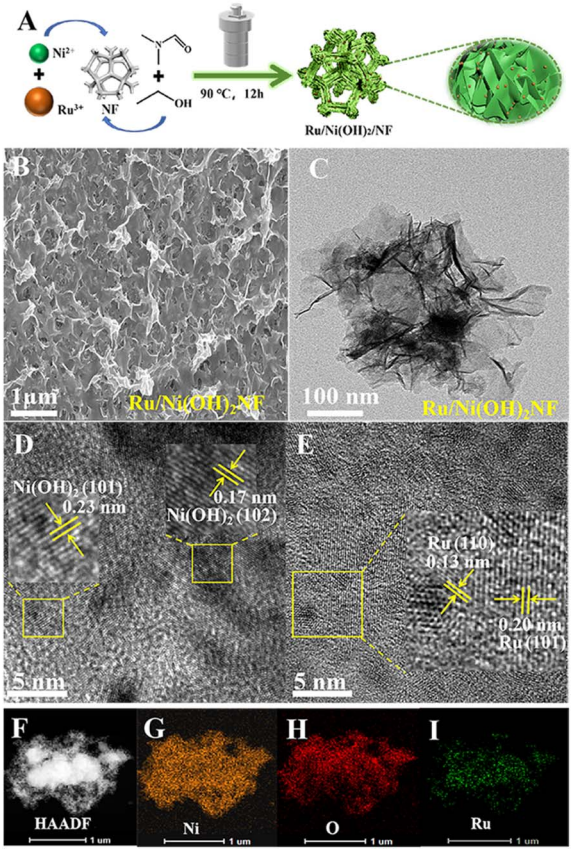

Fig. 1 Schematic illustration of the synthetic process of $Ru/Ni(OH)_2$/NF (A). SEM (B), HRTEM (C–E) and HAADF-STEM (F) images of $Ru/Ni(OH)_2$/NF and the corresponding elemental mapping images of (G) Ni, (H) O, and (I) Ru.

responsible for the lack of significant diffraction peaks in the XRD pattern.

The TEM image of the sample (Fig. 1C) exhibits a thin film structure, and the nearly transparent nature implies the ultra-thin dimension of the synthesized $Ni(OH)_2$ nanoflakes, which will play a vital function in the improvement of the catalytic performance.[19] As displayed in Fig. 1D, the lattice fringes with the spacing of 0.17 nm and 0.23 nm corresponded to the (1 0 2) and (1 0 1) planes of $Ni(OH)_2$, respectively. Meanwhile, the HRTEM images (Fig. 1E) show distinct lattice fringes with interplanar lengths of 0.20 and 0.13 nm that may be indexed to the (1 0 1) and (1 1 0) distinctive crystal plane of the hexagonal metallic Ru,[22,23] respectively. Meanwhile, a rich $Ru/Ni(OH)_2$ interface formed when several Ru nanoparticles coupled with $Ni(OH)_2$, as seen in Fig. S3.† Finally, the HAADF-STEM and elemental mapping images (Fig. 1F–I) show that only Ni, O and Ru are consistently diffused, which further supports that Ru dispersed well on the $Ni(OH)_2$ slices. This homogeneous distribution may facilitate the utilization of precious metals. A well-surfaced dispersed Ru cluster can improve the overall reaction dynamics. The EDS picture of the catalyst is shown in Fig. S4,† illustrates the less precious metals and further explains why no significant Ru diffraction peak appeared in the XRD pattern.

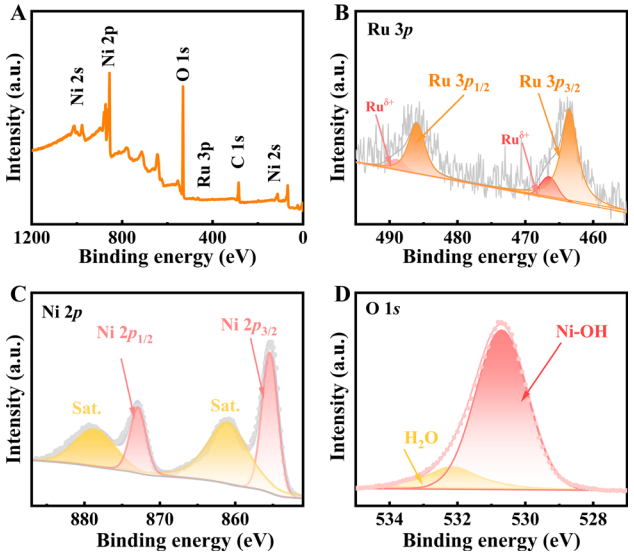

Fig. 2 XPS survey spectra (A) and narrow scan results of Ru 3p (B), Ni 2p (C), and O 1s (D) for $Ru/Ni(OH)_2$/NF.

XPS analysis was used to further identify the valence state of the chemical elements, as shown in Fig. 2. The XPS survey spectrum of the catalyst prove the presence of Ru, Ni and O elements (Fig. 2A). The valence state of Ru was confirmed to be Ru^0. The Ru 3p spectrum can be seen in Fig. 2B, where the two peaks of 463.2 eV and 485.4 eV can be ascribed to Ru $3p_{3/2}$ and Ru $3p_{1/2}$, respectively, which verifies the presence of Ru^0.[24] This manifests the position of the splitting peaks at 465.5 eV and 488.2 eV, consistent with $Ru^{\delta+}$.[25] As shown in Fig. 2C, the Ni 2p XPS spectrum can be fitted with two spin–orbit peaks of $Ni(OH)_2$ at 855.4 eV and 872.9 eV, which can be ascribed to Ni $2p_{3/2}$ and the Ni $2p_{1/2}$, respectively.[26,27] The creation of $Ni(OH)_2$ is shown by the shakeup satellite peak located at 860.9 eV and 878.6 eV.[28,29] The O 1s spectrum is displayed in Fig. 2D, and Ni–OH and H_2O were attributed to the peaks at 530.7 eV and 532.1 eV, also supporting the formation of $Ni(OH)_2$.[30–32]

3.2. Electrocatalytic performance for HER

The HER performance of the as-prepared varied catalysts was evaluated by a three-electrode system. The linear sweep voltammetry (LSV) curves of the catalysts are exhibited in Fig. 3A, where the $Ru/Ni(OH)_2$/NF catalyst (curve a in Fig. 3A) exhibits the best hydrogen evolution reaction performance. The HER of the best catalyst overpotential is 42 mV ($\eta_{10} = 42$ mV) to achieve 10 mA cm^{-2} (η_{10}). The LSV curve (curve b in Fig. 3A) of $Ni(OH)_2$/NF ($\eta_{10} = 229$ mV) can evaluate the effect of Ru on the catalytic activity, although it has a higher catalytic activity than the naked NF ($\eta_{10} = 305$ mV) (curve d in Fig. 3A); its catalytic performance is far lower than that of $Ru/Ni(OH)_2$/NF. It also suggests that Ru plays a crucial function in hybrid materials for HER. The HER capability of Ru on NF (Ru/NF) (curve c in Fig. 3A) is also examined, and at 10 mA cm^{-2}, Ru/NF had a larger overpotential of 187 mV than that of the best catalyst. It should be pointed out that pure $Ni(OH)_2$/NF does not have excellent HER

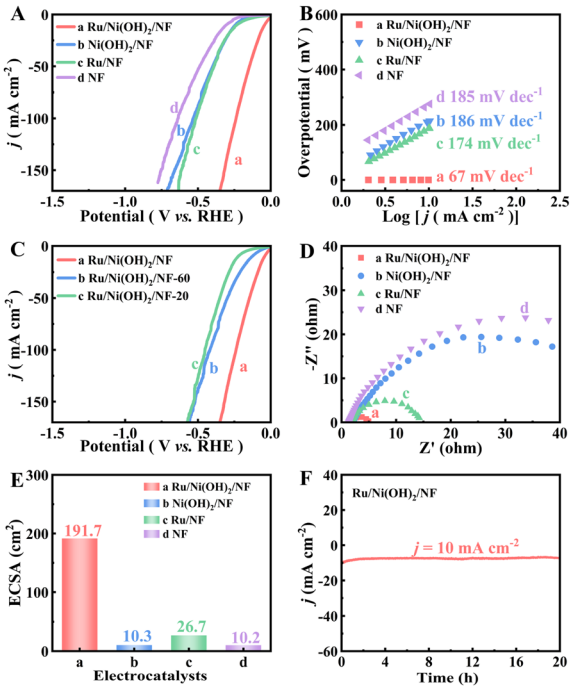

Fig. 3 The HER measurements in 1 M KOH at 5 mV s^{-1}. The LSV curves (A) and the Tafel fitting plots (B) of $Ru/Ni(OH)_2/NF$ (a), $Ni(OH)_2/NF$ (b), Ru/NF (c), and NF (d). The LSV curves (C) of $Ru/Ni(OH)_2/NF$ (a), $Ru/Ni(OH)_2/NF$-60 (b), and $Ru/Ni(OH)_2/NF$-20 (c). The Nyquist plots (D) and the ECSA (E) of $Ru/Ni(OH)_2/NF$ (a), $Ni(OH)_2/NF$ (b), Ru/NF (c), and NF (d). The *i*–*t* test of the $Ru/Ni(OH)_2/NF$ at a current density of 10 mA cm^{-2} (F).

performance; in view of the aforementioned facts, the activity of HER is due to the good synergistic effect between the nanosheet and the mono-metal Ru rather than the surface oxide of NF. In addition, through comparative analysis with several Ru-containing precious metal catalysts, our catalyst's activity is determined to be on par with or even superior to publicly published Ru-based catalysts (Table S1†).

Tafel slope is another important parameter for evaluating the reaction kinetics. The Tafel slope of $Ru/Ni(OH)_2/NF$ (67 mV dec^{-1}) is obvious smaller than that of other materials, indicating good reaction dynamics of the working electrode (Fig. 3B). In the HER process, the mechanism of the reaction and its rate-determining step for a catalyst can be approximately estimated based on its Tafel slope. Obviously, the $Ru/Ni(OH)_2/NF$ electrode exhibited a Tafel slope of 67 mV dec^{-1}, implying that the Volmer–Heyrovsky mechanism dominated during hydrogen production.[33–36]

In order to investigate the effect of the formation of $Ni(OH)_2$ on the HER catalytic performance, this work changed the amount of $NiCl_2 \cdot 6H_2O$ to optimize the morphology of the generated $Ni(OH)_2$. The relationship between the HER performance and the $Ni(OH)_2$ morphology is shown in Fig. 3C, and the $Ru/Ni(OH)_2/NF$ displays the highest HER activity. The morphology of the binding material can be testified, and the catalytic performance at a dosage of 20 mg is obviously worse than that at 40 mg. With the increase in the dosage (60 mg), the generated $Ni(OH)_2$ can result in accumulation or aggregation so that more active sites are covered, and thus the catalytic performance deteriorates. Therefore, the $Ru/Ni(OH)_2/NF$ synthesized under appropriate conditions has a stereoscopic morphology, which can expose more active sites and show the best catalytic activity of HER. In addition, the measured values of electrochemical impedance spectroscopy (EIS) are also important parameters to describe the kinetics and conductivity of catalysts. In the EIS (Fig. 3D), $Ni(OH)_2$ has a poor conductivity (49.8 Ω), and after doping Ru into the $Ni(OH)_2$ nanosheets, $Ru/Ni(OH)_2/NF$ has the smallest impedance value (5 Ω) in HER. It can be seen that the synergistic effect of Ru and $Ni(OH)_2$ can better regulate the electronic structure of the catalyst, optimize the energy barrier and accelerate the charge transfer rate of the catalytic reaction.

The electrochemically active surface area (ECSA), which may be subjectively determined from the double layer capacitance (C_{dl}) obtained from the cyclic voltammetry (CV) curve of the non-Faraday current zone, is another way to understand the HER electrocatalytic activity, as shown in Fig. S6.† By withdrawing the corresponding C_{dl}, the ECSA values of various samples were obtained, and it is clear that the $Ru/Ni(OH)_2/NF$ exhibits the highest ECSA value (Fig. 3E and S7†). The ECSA values of the $Ru/Ni(OH)_2/NF$, $Ni(OH)_2/NF$, Ru/NF and NF material were calculated to be 191.7, 10.3, 26.6 and 10.2 cm^2, respectively. The ECSA of Ru/NF is nearly twice than that of $Ni(OH)_2/NF$, indicating that Ru plays a crucial role in this material. Compared with catalysts with different $Ni(OH)_2$ morphology, $Ru/Ni(OH)_2/NF$ also showed the highest ECSA value, further indicating that the entangled $Ni(OH)_2$ surface layer is more conducive to the exposure of active sites so as to maximize the activity of the catalyst.

As depicted in Fig. S8,† for observing the effect of MeOH on HER, this work tested the HER ability of $Ru/Ni(OH)_2/NF$ at diverse MeOH concentrations, which found that the activity was comparable to that without MeOH in the electrolyte. This indicates that the introduction of MeOH has no obvious effect on the HER activity, and subsequently, it can be introduced into the anode instead of OER for electrolysis. Additionally, for the *i*–*t* measurement at a voltage of −1.07 V, the *i*–*t* curve of $Ru/Ni(OH)_2/NF$ did not change significantly after 20 h (Fig. 3F), indicating the excellent catalytic stability. Furthermore, the LSV curves of $Ru/Ni(OH)_2/NF$ do not fluctuate significantly before and after 1000 continuous long-term CV cycles (Fig. S5†). It can be well illustrated that $Ru/Ni(OH)_2/NF$ has remarkable durability and stability for HER.

3.3. Electrocatalytic performance for MOR

The MOR performance of the as-prepared varied catalysts was evaluated by a simple three-electrode system. The electrochemical oxidation of MeOH is fascinating because it can be transformed into value-added chemicals such as formate.[37] Firstly, the $Ru/Ni(OH)_2/NF$ performance of the electrodes is evaluated by the LSV test. It exhibits good MOR activity at a current density of 10 mA cm^{-2} (Fig. 4A); the anodic oxidation activity increases gradually with an increase in the MeOH

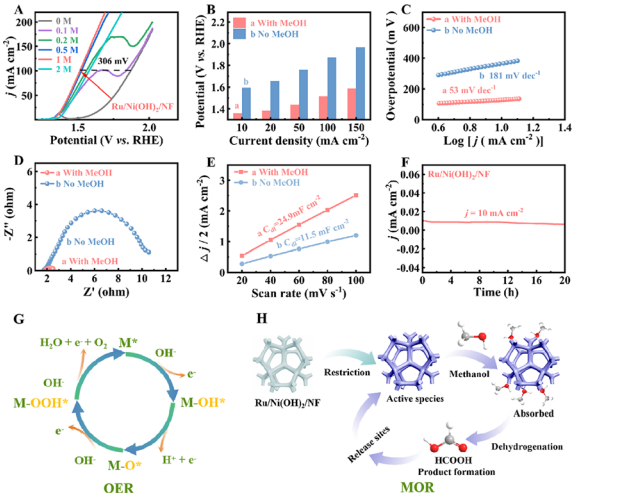

Fig. 4 The LSV curves of Ru/Ni(OH)$_2$/NF in 1 M KOH with 0 M, 0.1 M, 0.2 M, 0.5 M, 1 M, and 2 M methanol (A). Comparison of the anodic potential to achieve varied current densities using Ru/Ni(OH)$_2$/NF in 1 M KOH with (a) and without (b) 1 M methanol (B). Tafel plots, (C) Nyquist plots (D) and the C_{dl} (E) of the Ru/Ni(OH)$_2$/NF, respectively. The *i*–*t* test of the Ru/Ni(OH)$_2$/NF at a current density of 10 mA cm^{-2} (F). The typical mechanism pathways for the OER (G) and MOR (H).

concentration, and only 1.36 V *vs.* RHE potential is required when the methanol concentration is 1 M. On this basis, with the increase in the methanol concentration, the electrocatalytic activity shows the opposite trend. This result indicates that the methanol concentration is more appropriate at 1 M. This illogical tendency may be caused by oxidation products that stick to the surface of the material and impede the process. In 1 M KOH solution without methanol, the anode needs to be at a potential of 1.6 V *vs.* RHE to reach 10 mA cm^{-2}. Thus, 1 M MeOH is chosen as the ideal concentration in this study to enhance the MOR efficiency.

As expected, the MOR capability of Ru/Ni(OH)$_2$/NF is superior to other materials (Fig. S9A†). In the scenario where 1 M methanol is introduced, Ru/NF has an obvious oxidation peak in the range of 1.7–1.9 V *vs.* RHE, as shown in Fig. S9B,† indicating that there should be an OER competitive reaction at the same time as the occurrence of the MOR, which limits MOR catalysis.[37,38] The observation of Ni(OH)$_2$/NF reveals the absence of an OER competitive reaction during MOR, as shown in Fig. S9C,† suggesting that the presence of Ni(OH)$_2$ facilitates MOR. This is likely due to facile Ni(OH)$_2$ dissociation in alkaline solution, which also facilitates the formation of OH_{ads} and accelerates the reaction kinetics. Ni acts as the catalytic active center of MOR, and the presence of Ni(OH)$_2$ has a great effect on the MOR. Therefore, we compared the morphology of Ni(OH)$_2$ (Fig. S10†), which verifies that very much or very little Ni(OH)$_2$ coverage would worsen the MOR activity. The proper morphological structure facilitates the exposure of the active site. A suitable composition can improve the catalytic activity of the catalyst.

In order to further compare the advantages of introducing methanol, the difference between the presence and absence of methanol at diverse current densities is compared in Fig. 4B. At 100 mA cm^{-2}, in comparison with the high oxidation potential without MeOH (1.87 V), Ru/Ni(OH)$_2$/NF (1.515 V) exhibits excellent performance in MOR; the potential difference between the presence and absence of methanol is as high as 355 mV. In the study, the anodic potential in methanol solution is lower than that reported for the majority of electrochemically-aided water break down systems (Table S2†); the results show that the catalyst provides considerable potential for practical application. It is a promising strategy for methanol oxidation to replace traditional OER. As shown in Fig. 4C and S9D,† Ru/Ni(OH)$_2$/NF has a relatively low Tafel slope of 53 mV dec^{-1} in 1 M methanol, which is significantly smaller than that of OER (181 mV dec^{-1}), indicating that Ru/Ni(OH)$_2$/NF has a faster kinetic process in methanol. In addition, the Tafel slope of Ru/Ni(OH)$_2$/NF for the MOR process is lower than those of Ni(OH)$_2$/NF (83 mV dec^{-1}) and Ru/NF (67 mV dec^{-1}), suggesting the enhanced reaction kinetics of Ru/Ni(OH)$_2$/NF for the MOR.

According to the EIS in Fig. 4D, surprisingly, the impedance value for Ru/Ni(OH)$_2$/NF with MeOH is 0.47 Ω cm^{-2}, which is 22 times lower than that without MeOH (10.3 Ω cm^{-2}). Identically, it displays much smaller charge transfer resistance than the other three materials (Fig. S11†). The small resistance of the Ru/Ni(OH)$_2$/NF implies that the charge transfer process is faster under MeOH conditions, further demonstrating an outstanding electrical conductivity and fast charge transfer rate. It was also indicated that a good conductivity structure can improve the mass transfer of the catalyst, reduce the internal resistance of the material, and promote the catalytic activity of the MOR. Hence, it is feasible to use Ru/Ni(OH)$_2$/NF as an efficient electrocatalyst for MOR.

In the potential range of non-Faraday processes, the resulting CV curve is shown in Fig. S12.† As can be seen in Fig. 4E, the C_{dl} value for Ru/Ni(OH)$_2$/NF is 24.9 mF cm^{-2}, which is more than twice that without MeOH, illustrating that Ru/Ni(OH)$_2$/NF has more active sites to react with MeOH. Ru/Ni(OH)$_2$/NF displayed a higher C_{dl} value than other materials under the same conditions (Fig. S13†); the results show that Ru/Ni(OH)$_2$/NF has a unique high activity toward MOR, the largest electrochemical activity and the most exposed active sites under MeOH conditions, which further indicated that the combination of Ru and Ni(OH)$_2$ could maximize the catalytic activity of MOR. Furthermore, the *i*–*t* test was operated for 20 h (Fig. 4F), with negligible changes in the current density during the test (Fig. 4F), demonstrating its long-term stability and the robust catalytic durability for MOR. In addition, Fig. S14† shows the morphology of the Ru/Ni(OH)$_2$/NF after the HER and MOR test. The results show that the material still retains a similar morphology as that before the test, which further indicates its good structural stability.

Finally, according to the mechanism of the classical OER process (Fig. 4G) and the summary of existing work, the surface of Ni is easily oxidized to form NiOOH, which is the key active substance of MOR.[39–41] As a result, the MOR mechanism of the Ru/Ni(OH)$_2$/NF electrocatalyst was deduced, as shown in Fig. 4H. The active species was first formed under alkaline conditions, the adsorption state was formed after the

adsorption of methanol molecules, and finally the product formate was obtained by dehydrogenation.[10,40,42–45]

3.4. Electrochemical performance of the two-electrode system by integrating MOR with HER

The addition of 1 M methanol to Ru/Ni(OH)$_2$/NF did not negatively affect the HER activity, as shown in Fig. S8.† Therefore, considering Ru/Ni(OH)$_2$/NF for MOR and HER under alkaline circumstances, a methanol electrolyzer was built in a 1 M KOH solution containing 1 M methanol using Ru/Ni(OH)$_2$/NF as the anode and cathode (Ru/Ni(OH)$_2$/NF||Ru/Ni(OH)$_2$/NF). Fig. 5A compares the overall water splitting in 1 M KOH solution without (curve b in Fig. 5A) and with (curve a in Fig. 5A) 1 M methanol. At 10 mA cm^{-2}, only 1.45 V is required in 1 M KOH solution containing 1 M methanol, and 1.67 V (the conventional overall water splitting) is required in 1 M KOH solution without methanol. In addition, Ru/Ni(OH)$_2$/NF requires a relatively low potential applied, which is comparable to or even better than most reported bifunctional electrocatalysts (Fig. 5B and Table S3†).

Similarly, the performance of the Ru/Ni(OH)$_2$/NF||Ru/Ni(OH)$_2$/NF electrolytic cell also overmatches that of other electrolytic cells under an equal state (Fig. 5C). The *i*–*t* measurement was done at a voltage of 1.36 V, and the performance of Ru/Ni(OH)$_2$/NF is only mildly reduced at 10 mA cm^{-2} for the 20 h long-term test (Fig. 5D); it was hypothesized that methanol was consumed because the current increased significantly after the addition of a small amount of methanol. In other words, the catalyst can significantly improve the electrolytic efficiency of the electrolytic cell. This shows that the HER coupling with MOR can indeed replace the traditional electrolysis of water, and it is feasible to achieve energy-saving hydrogen production and electrochemical synthesis of value-added chemicals in parallel.

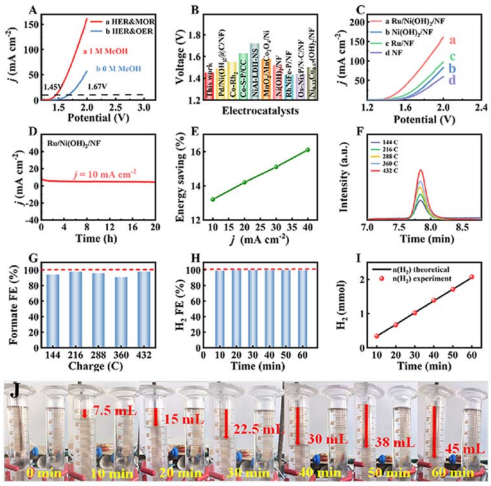

Fig. 5 The LSV curves in 1 M KOH with (a) and without (b) 1 M methanol for the Ru/Ni(OH)$_2$/NF||Ru/Ni(OH)$_2$/NF system (A). The histogram comparing the electrochemical performance of the as-synthesized catalyst with that of the reported catalysts at 10 mA cm^{-2} (B). The LSV curves of Ru/Ni(OH)$_2$/NF||Ru/Ni(OH)$_2$/NF (a), the Ni(OH)$_2$/NF||Ni(OH)$_2$/NF (b), Ru/NF||Ru/NF (c) and NF||NF (d) in 1 M KOH solution with 1 M methanol (C). The *i*–*t* curve of the Ru/Ni(OH)$_2$/NF||Ru/Ni(OH)$_2$/NF at 10 mA cm^{-2} for 20 h (D). The energy consumption savings of HER & MOR at different current densities (E). The HPLC measurements (144C, 216C, 288C, 360C, and 432C; the numbers represent the electrolysis charge) of methanol oxidation to formate in 1 M KOH with 1 M methanol (F). The FE for formate production at the anode (G) and H_2 on the cathode (H), respectively. The measured H_2 amount and theoretical values (I). At different times, the corresponding cylinder diagram of hydrogen production (J).

Meanwhile, during the *i*–*t* test in the methanol electrolyzer, many bubbles can be obviously observed in the cathode, but there is no obvious bubble in the anode, as shown in Movie S1 of the ESI,† which means that no competing OER occurred in this process. Another crucial factor is energy efficiency, which it can be represented by the percentage of energy input to the produced product.[44] By comparing the electrolysis of water with the electrolysis of methanol across different levels of current density and analyzing the ratio between current and voltage, one can ascertain the extent of energy conservation. The data presented in Fig. 5E illustrates that the energy conservation rates of 13.2%, 14.2%, 15.1%, and 16.1% can be attained at current densities of 10, 20, 30, and 40 mA cm^{-2}, respectively. When the current density rises, the energy consumption of HER and MOR is more effective. It shows that not only energy saving but value addition can also be achieved, which is a win–win situation. In the HPLC test results, only a single signal was observed, indicating that only one substance was present in the solution. As the amount of charge increases, the signal strength gradually increases (Fig. 5F). The retention time is consistent with the standard material of formate, indicating that the product is formate (Fig. S15†). The resulting formate Faraday efficiency averaged about 95% (Fig. 5G), which proved that Ru/Ni(OH)$_2$/NF has strong catalytic activity in the process of formate conversion, reflecting the high selectivity of Ru/Ni(OH)$_2$/NF for MOR.

Additionally, the Faraday efficiency of the Ru/Ni(OH)$_2$/NF couple's ability to produce H_2 was assessed every 10 min using the water displacement technique. The experiment was completed in 1 hour because of the limited volume of the cylinder. The volume of the anode does not change, indicating that no gas is produced in the anode, in line with the estimated situation. H_2 generation in the methanol electrolyzer can reach a high Faraday efficiency of 99% (Fig. 5H), which is close to the theoretical calculation value (Fig. 5I). The measurement process of H_2 is shown in Fig. 5J. In view of the previous findings, the Ru/Ni(OH)$_2$/NF catalyst is advantageous due to its simple, high efficiency and stability. Importantly, it has high selectivity for MOR, produces only one product format, and can turn cheap products into value-added products, indicating that it has significant application potential as a dual-function electrode.

Ru/Ni(OH)$_2$/NF exhibits excellent electrocatalysis in alkaline solutions, which may be attributed to: (1) the Ni(OH)$_2$ morphology. On the one hand, it is easy to form affinity-building OH_{ads} in alkaline conditions, promoting electrocatalytic reaction activity. On the other hand, the Ni(OH)$_2$ surface booming overlay or too little will results in poor conductivity. It was found that a good structure–activity relationship can optimize the catalytic energy level, increase charge

transfer rate, reduce the reaction energy barrier, and accelerate the reaction kinetics.[46] (2) Strong synergies between $Ni(OH)_2$ and Ru. The activity of Ru/NF and $Ni(OH)_2$/NF is ordinary. The ECSA value of Ru/$Ni(OH)_2$/NF was 18.6 times that of unmodified $Ni(OH)_2$. The results show that the synergistic effect of $Ni(OH)_2$ and Ru promotes the enrichment of active species, greatly reduces the reaction drive potential, and lowers the reaction energy consumption, which showed excellent electrocatalytic activity.

4 Conclusions

In summary, we successfully synthesized Ru/$Ni(OH)_2$/NF bifunctional catalysts by a one-step hydrothermal method. It exhibits a large electrochemically active surface area and demonstrates excellent MOR and HER electrochemical performance under alkaline conditions. At a current density of 10 mA cm^{-2}, the overpotentials for HER is 42 mV, and the potential for MOR is 1.36 V *vs.* RHE, respectively, showing fast reaction kinetics and excellent stability (20 h). Moreover, the methanol electrolysis cell only requires a voltage of 1.45 V to achieve a current density of 10 mA cm^{-2}. This strategy not only enables the highly selective oxidation of methanol to the value-added chemical formate but also achieves the production of high-purity hydrogen with 100% FE, with the energy efficiency exceeding 10% compared to traditional electrolysis hydrogen production systems, which has some economic value. This study demonstrates that MOR instead of OER coupled with HER can achieve the co-production of formate and hydrogen, providing a new direction for the development of novel electrochemical hydrogen production technologies.

Author contributions

Jiajie Lin: investigation, methodology, conceptualization, validation, data curation, writing – original draft, formal analysis. Jie Chen: methodology, formal analysis, validation. Changhui Tan: resources, writing – review & editing. Yingzhen Zhang: visualization, conceptualization, writing – review & editing. Yancai Li: conceptualization, funding acquisition, resources, writing – review & editing, supervision.

Conflicts of interest

The authors state that none of the work presented in this study may have been influenced by any known conflicting financial interests or personal ties.

Acknowledgements

The research was conducted with support from the National Natural Science Foundation of China (21905125) and the Natural Science Foundation of Fujian province in China (No. 2020J01802).

Notes and references

1 Y. Zhao, S. H. Xing, X. Y. Meng, J. H. Zeng, S. B. Yin, X. F. Li and Y. Chen, *Nanoscale*, 2019, **11**, 9319–9326.
2 R. T. Parayil, S. K. Gupta, M. Pal, A. Dutta, D. Tyagi, K. Sudarshan and M. Mohapatra, *RSC Adv.*, 2023, **13**, 31101–31111.
3 Y. X. Sun, A. J. Huang, Z. J. Li, Y. Q. Fu and Z. G. Wang, *Electrocatalysis*, 2022, **13**, 494–501.
4 Z. Y. Wu, F. Y. Chen, B. Y. Li, S. W. Yu, Y. Z. Finfrock, D. M. Meira, Q. Q. Yan, P. Zhu, M. X. Chen, T. W. Song, Z. Y. Yin, H. W. Liang, S. Zhang, G. F. Wang and H. T. Wang, *Nat. Mater.*, 2023, **22**, 100–108.
5 P. J. Wang, Y. T. Yan, P. C. Wang, Z. Y. Ye, X. H. Zheng and W. Cai, *Chem. Eng. J.*, 2023, **455**, 140856.
6 Y. Y. Song, J. L. Cheng, J. Liu, Q. Ye, X. Gao, J. J. Lu and Y. L. Cheng, *Appl. Catal., B*, 2021, **298**, 120488.
7 C. Q. Li, S. W. Kim, H. Y. Lim, Q. K. Sun, Y. Jiang, H. J. Noh, S. J. Kim, J. Baek, S. K. Kwak and J. B. Baek, *Adv. Mater.*, 2023, **35**, 01369.
8 T. Liu, A. R. Li, C. B. Wang, W. Zhou, S. J. Liu and L. Guo, *Adv. Mater.*, 2018, **30**, 1803590.
9 J. L. Du, D. L. Xiang, K. X. Zhou, L. C. Wang, J. Y. Yu, H. H. Xia, L. L. Zhao, H. Liu and W. J. Zhou, *Nano Energy*, 2022, **104**, 107875.
10 J. S. Li, L. M. Li, J. Wang, A. Cabot and Y. F. Zhu, *ACS Energy Lett.*, 2024, **9**, 853–879.
11 J. M. Wang, B. X. Zhang, W. Guo, L. Wang, J. Chen, H. G. Pan and W. P. Sun, *Adv. Mater.*, 2023, **35**, 2211099.
12 B. You, X. Liu, N. Jiang and Y. J. Sun, *J. Am. Chem. Soc.*, 2016, **138**, 13639–13646.
13 H. Chen, J. Zhang, R. Wan, X. Zhang, Q. Pan, M. Li and B. Chen, *RSC Adv.*, 2024, **14**, 9109–9113.
14 J. C. Zhang, Y. N. Gu, Y. Lu, C. C. Zhu, G. C. Liu, C. Wang, D. M. Sun, Y. W. Tang and H. J. Sun, *Appl. Catal., B*, 2023, **325**, 122316.
15 J. Zhang, P. Liu, G. Wang, P. P. Zhang, X. D. Zhuang, M. W. Chen, I. M. Weidinger and X. L. Feng, *J. Mater. Chem. A*, 2017, **5**, 25314–25318.
16 C. Ling, H. B. Li, C. Z. Yuan, Z. K. Yang, H. B. Chong, X. J. Qian, X. J. Lu, T. Y. Cheang and A. W. Xu, *Catal. Sci. Technol.*, 2021, **11**, 3865–3872.
17 M. A. R. Anjum, M. S. Okyay, M. Kim, M. H. Lee, N. Park and J. S. Lee, *Nano Energy*, 2018, **53**, 286–295.
18 X. K. Wu, Z. C. Wang, D. Zhang, Y. N. Qin, M. H. Wang, Y. Han, T. R. Zhan, B. Yang, S. X. Li, J. P. Lai and L. Wang, *Nat. Commun.*, 2021, **12**, 4018.
19 R. Narasimman, M. Waldiya, K. Jalaja, S. K. Vemuri, I. Mukhopadhyay and A. Ray, *Int. J. Hydrogen Energy*, 2021, **46**, 7759–7771.
20 M. X. Zhong, M. J. Xu, S. Y. Ren, W. M. Li, C. Wang, M. B. Gao and X. F. Lu, *Energy Environ. Sci.*, 2024, **17**, 1984–1996.
21 W. Chen, X. Zhu, R. Wang, W. Wei, M. Liu, S. Dong, K. K. Ostrikov and S. Q. Zang, *J. Energy Chem.*, 2022, **75**, 16–25.

22 Y. L. Wu, X. F. Li, Y. S. Wei, Z. M. Fu, W. B. Wei, X. T. Wu, Q. L. Zhu and Q. Xu, *Adv. Mater.*, 2021, **33**, 2006965.
23 K. Tu, D. Tranca, F. Rodríguez Hernández, K. Jiang, S. Huang, Q. Zheng, M. X. Chen, C. Lu, Y. Su, Z. Chen, H. Mao, C. Yang, J. Jiang, H. W. Liang and X. Zhuang, *Adv. Mater.*, 2020, **32**, 2005433.
24 Z. Liu, X. D. Yang, G. Z. Hu and L. G. Feng, *ACS Sustain. Chem. Eng.*, 2020, **8**, 9136–9144.
25 J. H. Luo, J. Wang, Y. Guo, J. W. Zhu, H. H. Jin, Z. W. Zhang, D. J. Zhang, Y. S. Niu, S. G. Hou, J. M. Du, D. P. He, Y. L. Xiong, L. Chen, S. C. Mu and Y. H. Huang, *Appl. Catal., B*, 2022, **305**, 121043.
26 B. Lv, X. Feng, X. Xi, X. Feng, Z. Yuan, Y. Yang and F. Zhang, *J. Colloid Interface Sci.*, 2021, **601**, 177–185.
27 L. H. Zhu, J. J. Cui, H. Zhang, L. Ruan, N. Ma, L. X. Zou, T. Deng, B. H. Chen and Q. Xiao, *ChemCatChem*, 2019, **11**, 3109–3116.
28 H. Krishna Sadhanala, I. Perelshtein and A. Gedanken, *ChemistrySelect*, 2020, **5**, 9626–9634.
29 H. Qin, X. L. Miao, D. D. Song, Y. T. Li, Y. N. Shen, J. J. Tang, Y. N. Qu, Y. C. Cao, L. L. Wang and B. J. I. Wang, *Ionics*, 2019, **25**, 3179–3188.
30 H. A. Zhao, L. T. Zhang, L. M. Dai, F. L. Yao, Y. Huang, J. Y. Deng, Y. S. Fu, J. W. Zhu and J. W. Sun, *Appl. Surf. Sci.*, 2022, **592**, 153252.
31 H. T. Wang, H. Y. Zou, Y. Y. Liu, Z. L. Liu, W. S. Sun, K. A. Lin, T. L. Li and S. J. Luo, *Sci. Rep.*, 2021, **11**, 21414.
32 F. N. I. Sari, C. Lin and J. M. Ting, *Chem. Eng. J.*, 2019, **368**, 784–794.
33 Q. Q. Chen, X. Yang, C. C. Hou, K. Li and Y. Chen, *J. Mater. Chem. A*, 2019, **7**, 11062–11068.
34 C. X. Sun, T. L. Wang, C. W. Sun and F. Li, *Int. J. Hydrogen Energy*, 2022, **47**, 19609–19618.
35 X. Y. Tian, P. C. Zhao and W. C. Sheng, *Adv. Mater.*, 2019, **31**, 1808066.
36 L. N. Sha, J. L. Yin, K. Ye, G. Wang, K. Zhu, K. Cheng, J. Yan, G. L. Wang and D. X. Cao, *J. Mater. Chem. A*, 2019, **7**, 9078–9085.
37 Q. Qian, X. He, Z. Li, Y. Chen, Y. Feng, M. Cheng, H. Zhang, W. Wang, C. Xiao, G. Zhang and Y. Xie, *Adv. Mater.*, 2023, **35**, 2300935.
38 H. B. Tao, Y. H. Xu, X. Huang, J. Z. Chen, L. J. Pei, J. M. Zhang, J. G. Chen and B. Liu, *Joule*, 2019, **3**, 1498–1509.
39 Y. C. Wang, M. Zhang, Y. Y. Liu, Z. K. Zheng, B. Y. Liu, M. Chen, G. Q. Guan and K. Yan, *Adv. Sci.*, 2023, **10**, 2207519.
40 Q. Z. Qian, X. Y. He, Z. Y. Li, Y. X. Chen, Y. F. Feng, M. Y. Cheng, H. K. Zhang, W. T. Wang, C. Xiao, G. Q. Zhang and Y. Xie, *Adv. Mater.*, 2023, **35**, 2300935.
41 W. Chen, Y. Y. Wang, B. B. Wu, J. Q. Shi, Y. Y. Li, L. T. Xu, C. Xie, W. Zhou, Y. C. Huang, T. H. Wang, S. Q. Du, M. L. Song, D. D. Wang, C. Chen, J. Y. Zheng, J. Liu, C. L. Dong, Y. Q. Zou, J. Chen and S. Y. Wang, *Adv. Mater.*, 2022, **34**, 2105320.
42 B. T. Zhu, B. Dong, F. Wang, Q. F. Yang, Y. P. He, C. J. Zhang, P. Jin and L. Feng, *Nat. Commun.*, 2023, **14**, 1686.
43 K. Deng, P. Liu, X. S. Liu, H. J. Li, W. Tian and J. Y. Ji, *Green Chem.*, 2023, **25**, 9837–9846.
44 J. Hao, J. W. Liu, D. Wu, M. X. Chen, Y. Liang, Q. Wang, L. Wang, X. Z. Fu and J. L. Luo, *Appl. Catal., B*, 2021, **281**, 119510.
45 G. Ma, X. Y. Zhang, G. F. Zhou and X. Wang, *Chem. Eng. J.*, 2021, **411**, 128292.
46 C. Li, H. Wen, P. P. Tang, X. P. Wen, L. S. Wu, H. B. Dai and P. Wang, *ACS Appl. Energy Mater.*, 2018, **1**, 6040–6046.